Electronic Supplementary Material (ESI) for Energy & Environmental Science.

Supporting Information for

Morphodynamics of dendrite growth in alumina based all solid-state sodium metal batteries†

Lin Geng, Dingchuan Xue, Jingming Yao, Qiushi Dai, Haiming Sun, Dingding Zhu, Zhaoyu Rong, Ruyue Fang, Xuedong Zhang, Yong Su, Jitong Yan, Stephen J. Harris, Satoshi Ichikawa, Liqiang Zhang,* Yongfu Tang,* Sulin Zhang* and Jianyu Huang*

Corresponding Author

**To whom correspondence should be addressed. E-mail: liqiangzhang85@163.com; tangyongfu@ysu.edu.cn; suz10@psu.edu; jyhuang8@hotmail.com*

Supplementary Movies

Description of Movie S1

An *in situ* optical microscopy movie showing the deposition/stripping of Na dendrites in β''-Al_2O_3 SE **(Fig. 1a-h**). The Na dendrites first nucleated and grew from the right electrode during electrochemical cycling. With increase of current densities, Na dendrites started to nucleate and grow on the left electrode as well. When the dendrites from the left and right electrodes met in the middle section of the β''-Al_2O_3 SE, short circuit took place. The movie was recorded at 25 frames/second and played at 56× speed.

Supplementary Figures

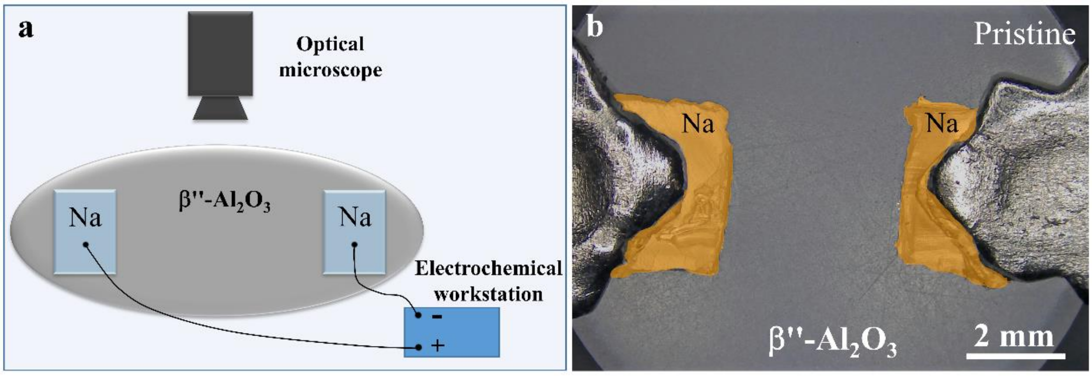

Fig. S1 *In situ* optical observations of Na deposition in SE. (a) Schematic of the *in situ* optical testing setup. (b) Optical microscopy image of the Na/β''-Al_2O_3/Na symmetric cell before cycling.

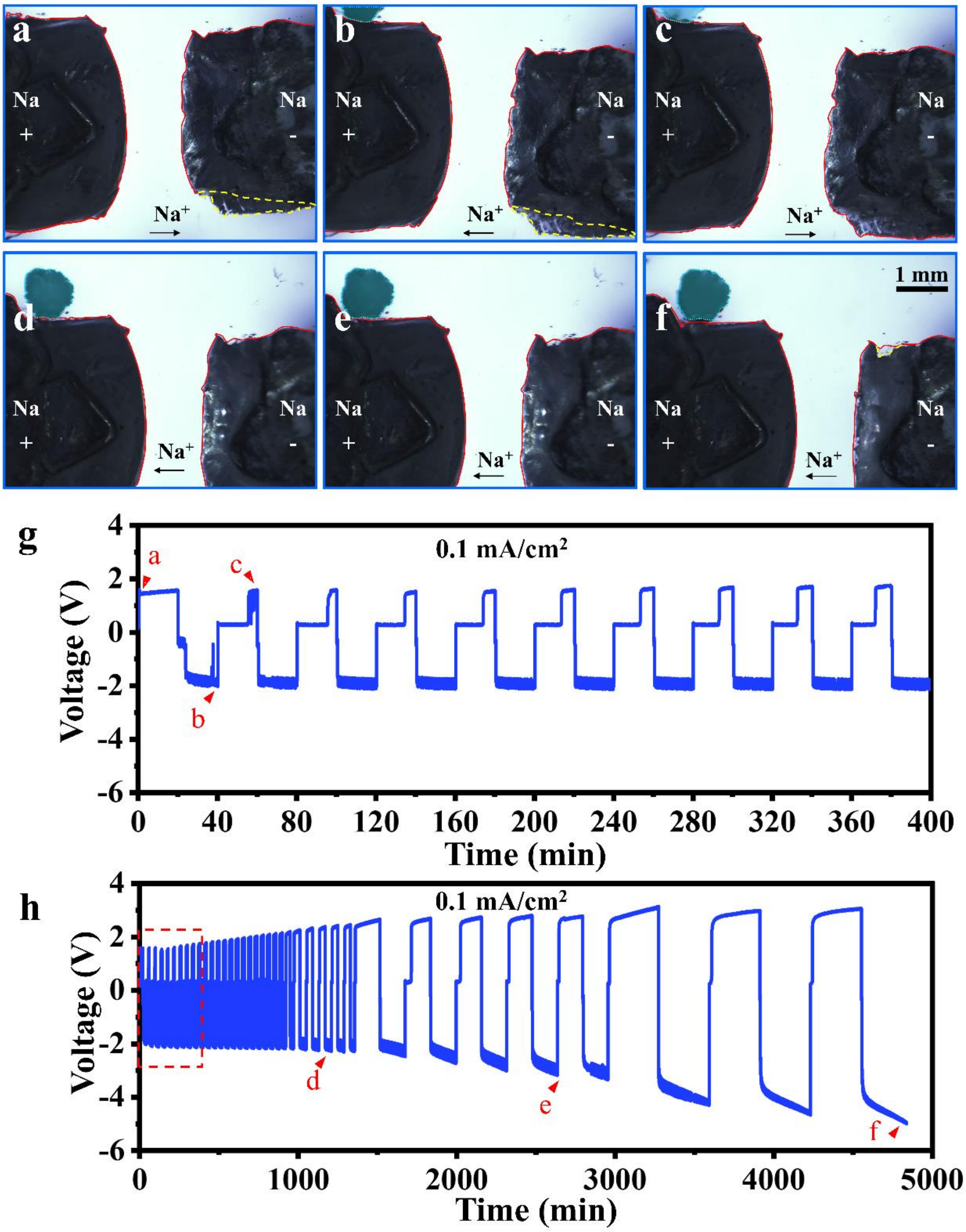
a
b
c
d
e
f
g
h
Na
+
-
Na⁺
1 mm
0.1 mA/cm²
Voltage (V)
Time (min)
4
2
0
-2
-4
-6
0
40
80
120
160
200
240
280
320
360
400
1000
2000
3000
4000
5000

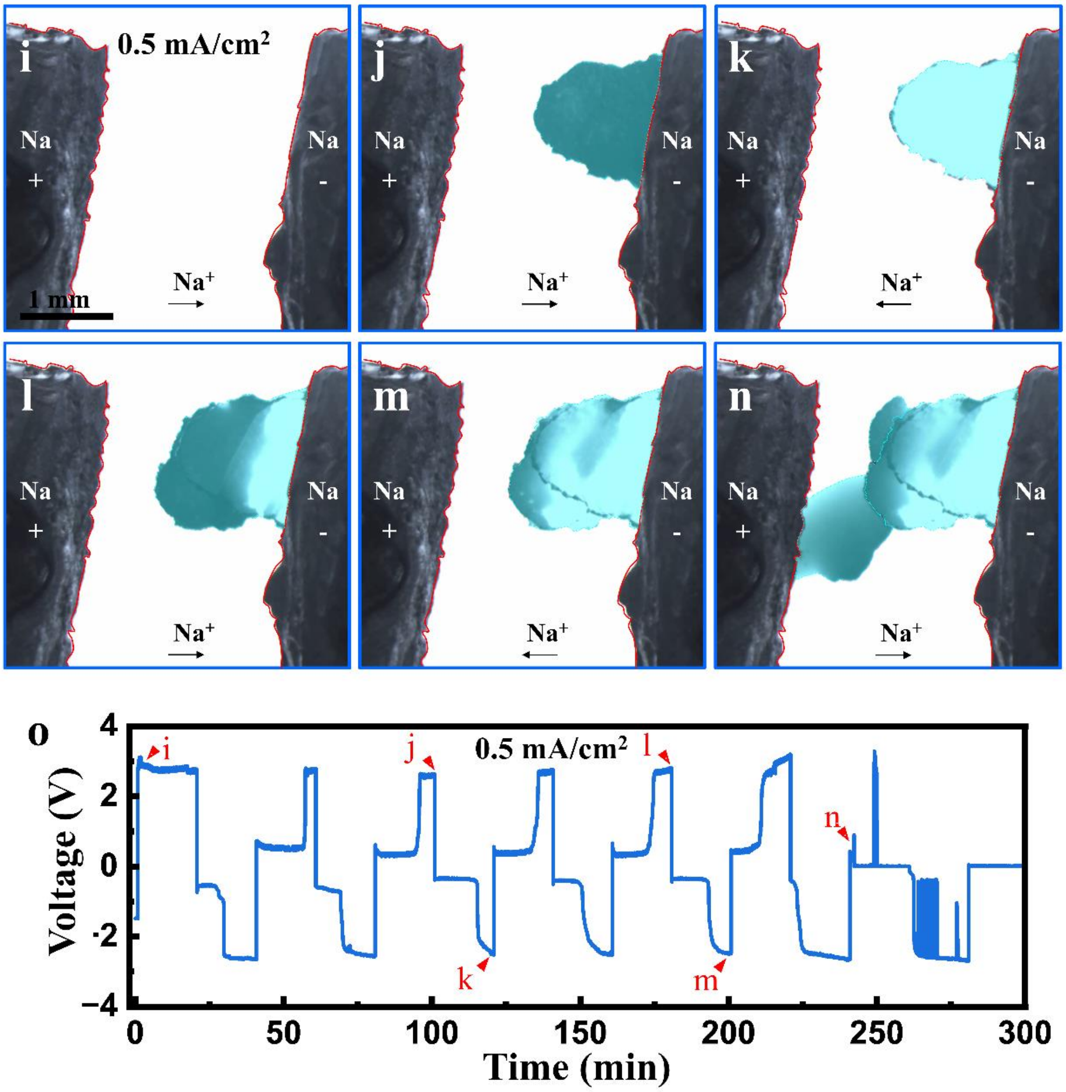
i
0.5 mA/cm²
Na
+
Na
-
Na⁺
1 mm
j
k
l
m
n
o
0.5 mA/cm²
Voltage (V)
Time (min)
4
2
0
-2
−4
0
50
100
150
200
250
300

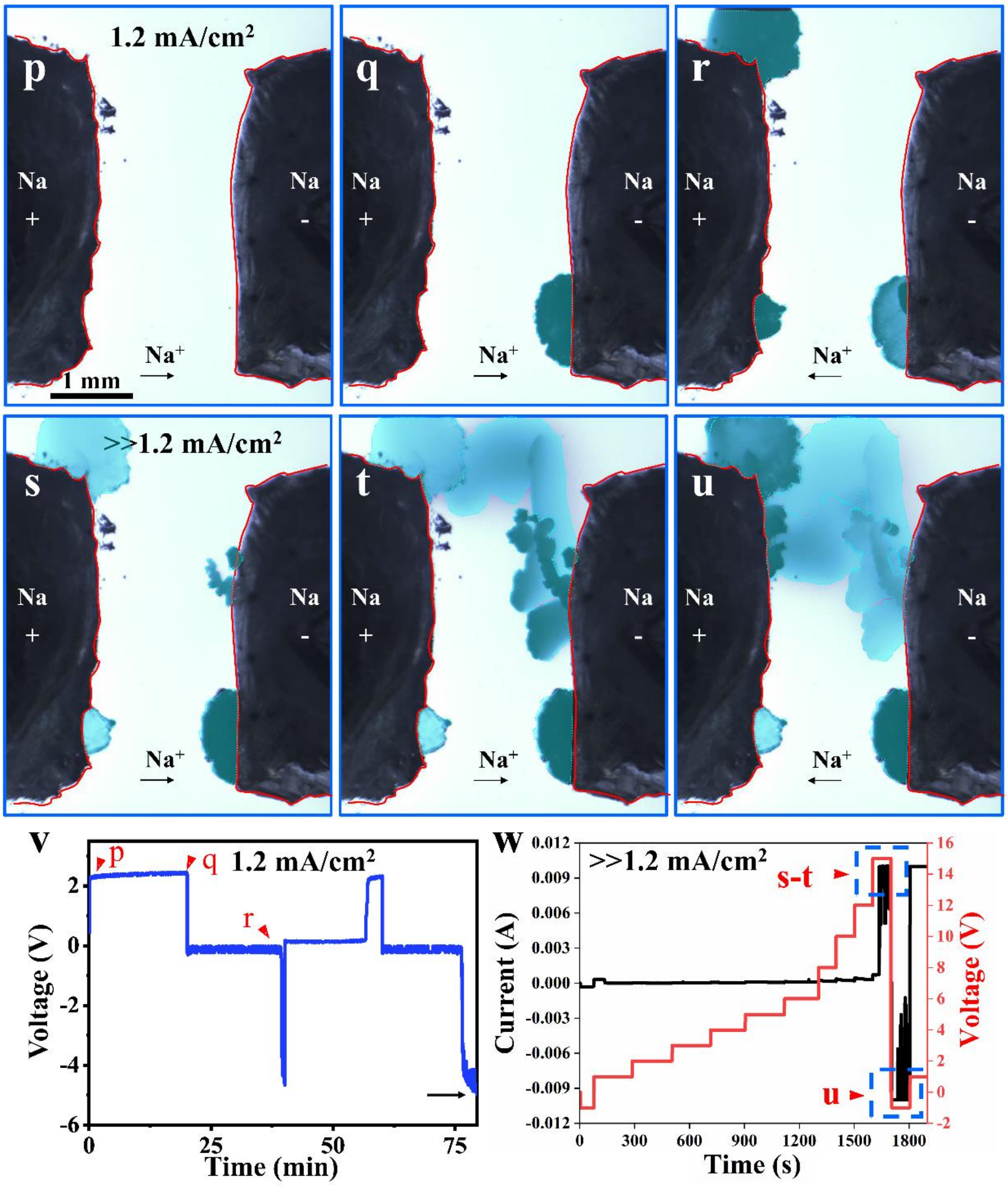

Fig. S2 ***In situ*** **optical microscopy visualization of Na dendrite growth in β''-Al_2O_3 SE in Na/β''-Al_2O_3/Na symmetric cells under different current densities.** (a-f) *In situ* observation of the dynamics of Na dendrite growth at a current density of 0.1 mA/cm^2. (g) Voltage and current recorded concurrently during *in situ* battery testing corresponding to the first ten cycles. (h) Voltage and current recorded concurrently during the whole cycles. (i-n) *In situ* observation of the dynamics of Na dendrite growth at a current density 0.5 mA/cm^2. (o) Voltage and current recorded concurrently during *in situ* battery testing. (p-u) *In situ* observation of the dynamics of Na dendrite growth. (v-w) Voltage and current recorded concurrently during *in situ* battery testing. A larger current density was applied in s-u.

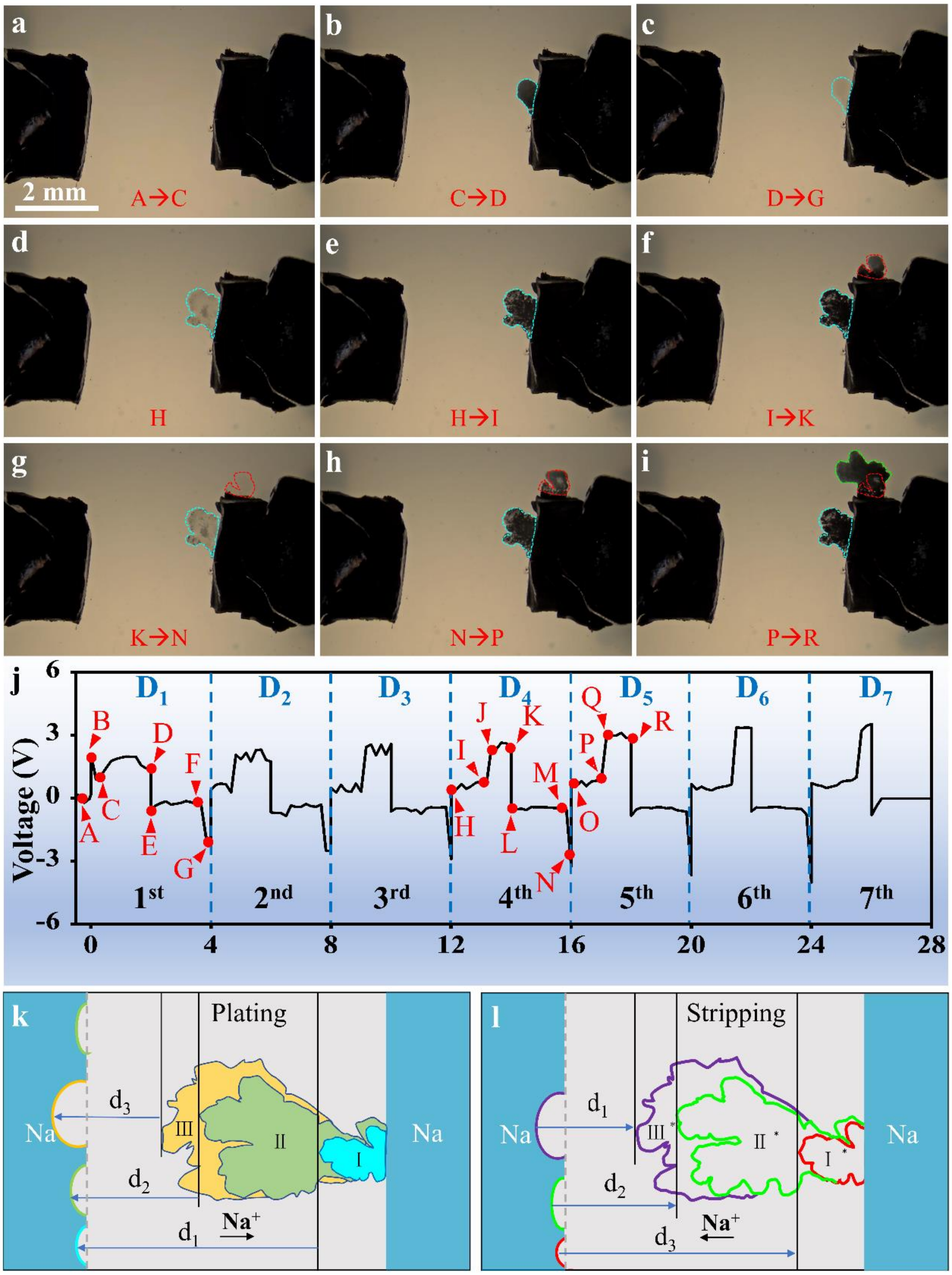

Fig. S3 Morphology evolution of the Na dendrites in a Na/β''-Al_2O_3/Na cell with the corresponding voltage and current profile. (a) Morphology of the pristine electrode before Na plating, corresponding to A→C in (j). (b) Na dendrite growth on the right electrode (blue dashed line), corresponding to C→D in (j). (c) Na dendrite stripping on the right electrode (blue dashed line), corresponding to D→G in (j). (d) Morphology of the right electrode after three plating/stripping cycles, corresponding to "H" in (j). The blue dashed line outlines the dendrite contour. (e) Na dendrite growth along the previous path as shown in (d), corresponding to H→I in (j). (f) Na dendrite growth in a new location (red dashed line outlines the contour), corresponding to I→K in (j). (g) Morphology of the right electrode after Na dendrite stripping, corresponding to K→N in (j). Blue and red dashed lines outline the stripping path. (h) Na dendrite growth along the previous path as shown in (g), corresponding to N→P in (j). (i) Na dendrite growth in a new path (green dashed line), corresponding to P→R in (j). (j) Voltage and current recorded concurrently during *in situ* battery testing. The current density in D_1-D_7 is 0.1, 0.2, 0.4, 0.6, 0.8, 1.0 and 1.2 mA/cm^2, respectively. (k-l) Schematic of the distance change during the plating and stripping process.

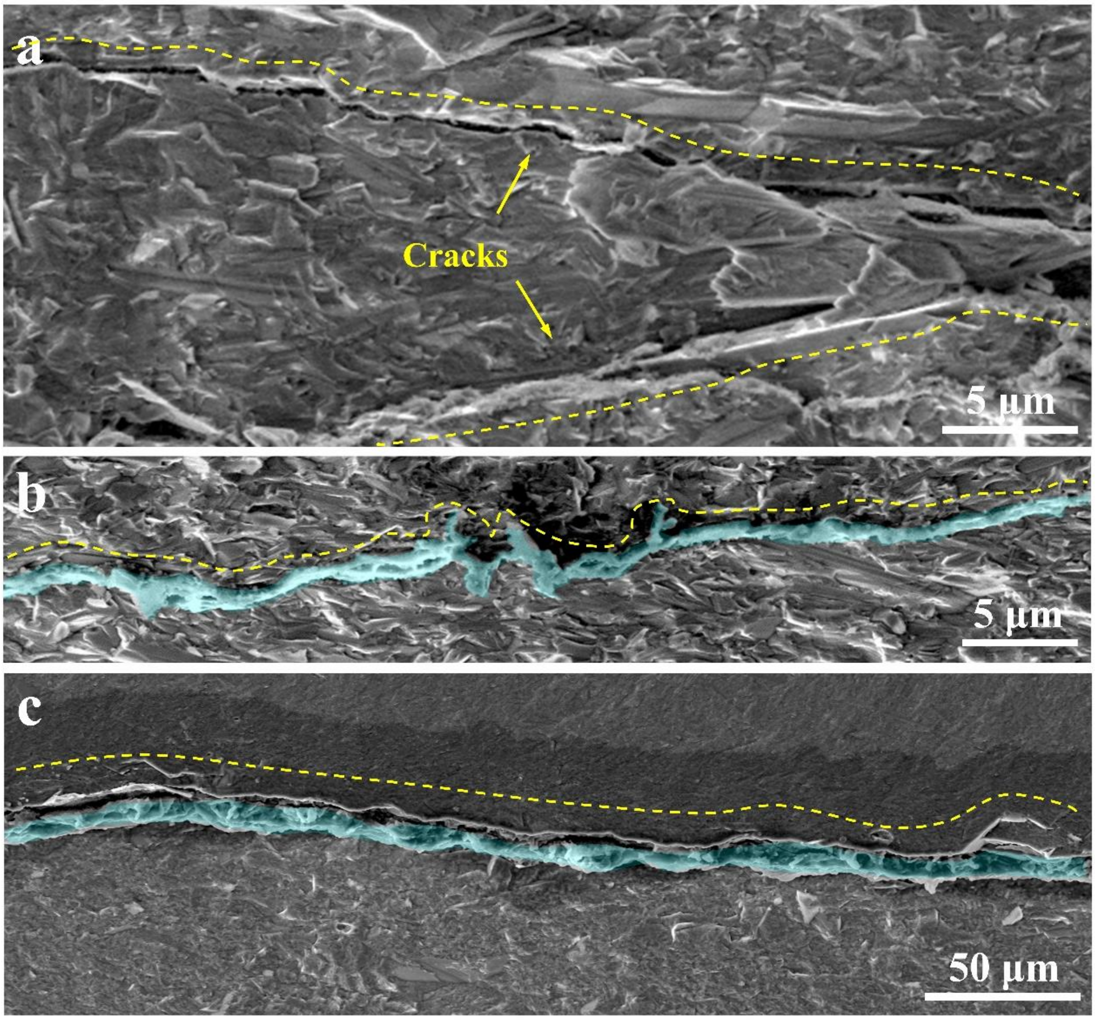

Fig. S4 SEM characterization of the β''-Al2O3 SE after in situ OM cycling. (a) A SEM image showing cross-sectional view of the crack. (b-c) SEM images of the Na filled crack. The yellow dashed lines trace the crack paths. The false color images mark Na metal.

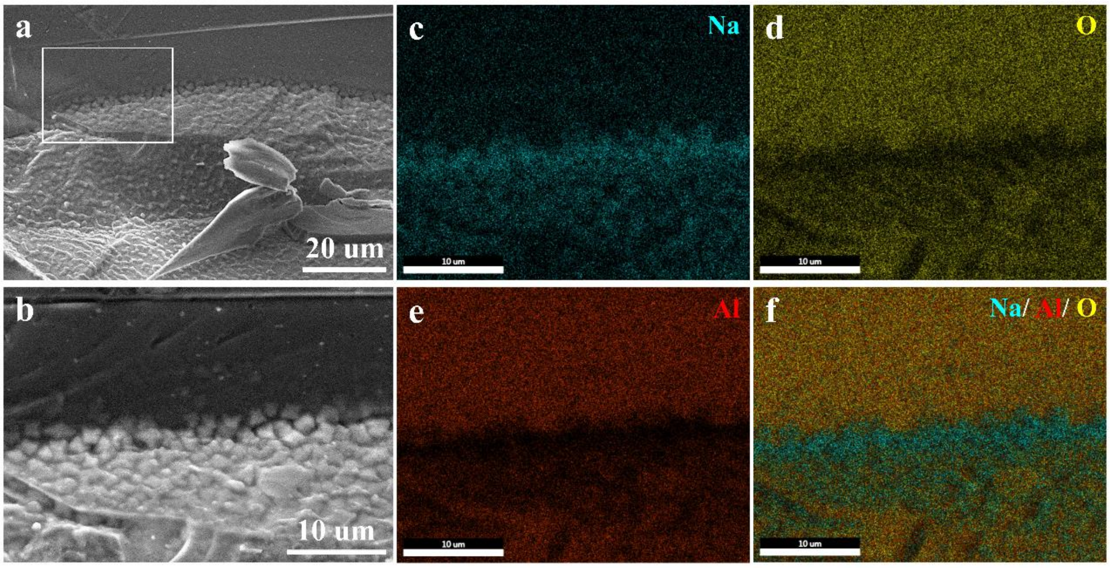

Fig. S5 SEM characterization of the β''-Al_2O_3 SE after cycling. (a) A SEM image showing cross-sectional view of the Na dendrites. (b) Magnified view of the Na and β''-Al_2O_3 interface corresponding to the boxed region in (a), (c-f) Elemental mapping images of the web-structured Na in β''-Al_2O_3 SE.

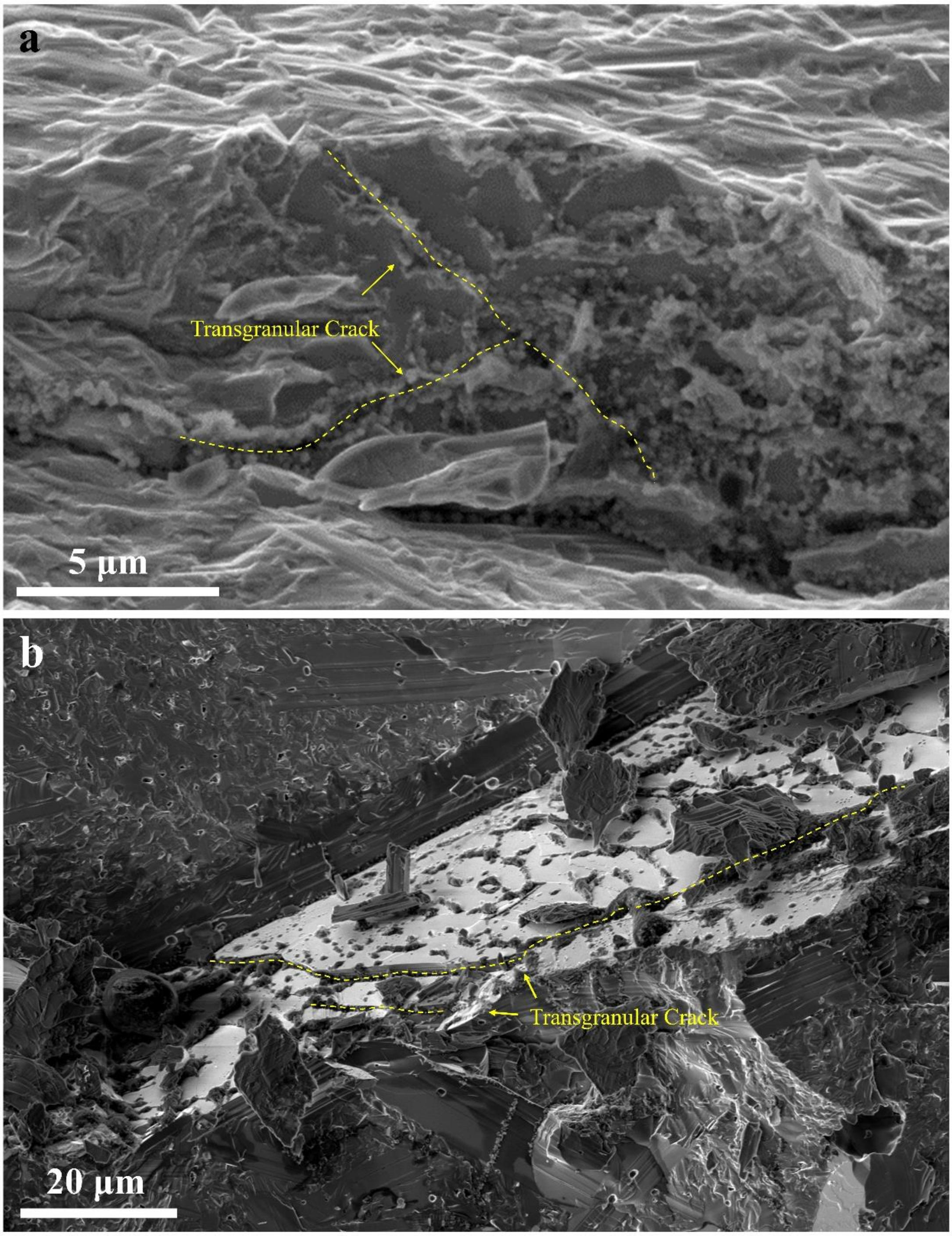

Fig. S6 Morphology of the β''-Al_2O_3 SE after optical cycling. (a,b) Magnified view of the web shaped Na and transgranular crack (outlined by yellow dotted lines) on the surface of a single crystal grain.

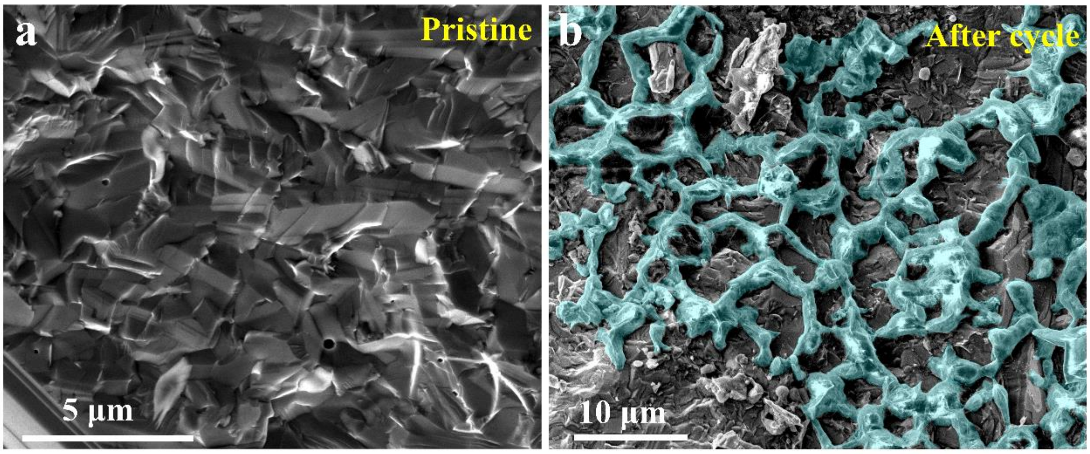

Fig. S7 Morphology of the polycrystalline β''-Al_2O_3 SE before and after cycling. (a) A SEM image showing the initial polycrystalline β''-Al_2O_3 grains. (b) A SEM image showing web-structured Na dendrites resided on the surface of polycrystalline β''-Al_2O_3 grains.

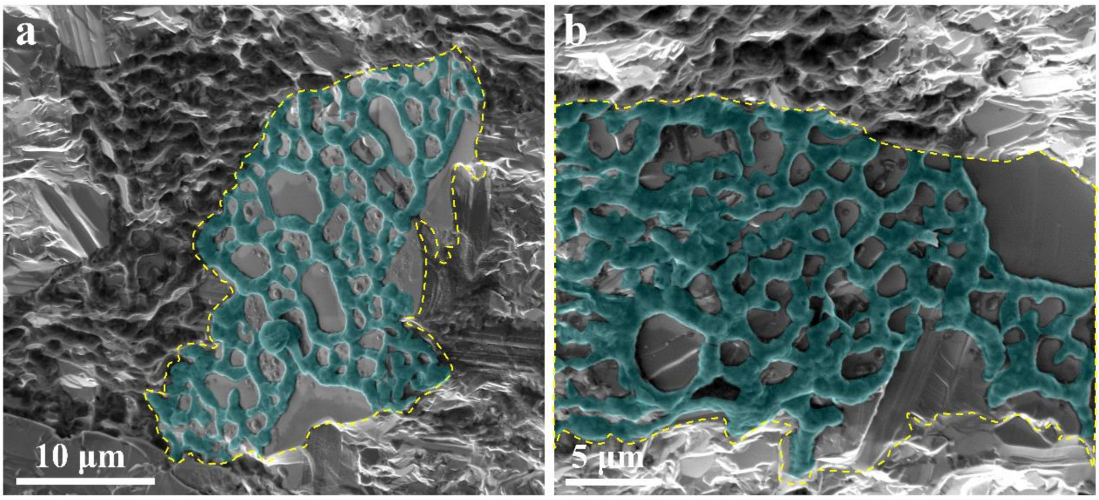

Fig. S8 Morphology of the β''-Al_2O_3 SE after cycling. (a-b) A SEM image showing web-structured Na dendrites resided on the surface of single crystal β''-Al_2O_3 grain.

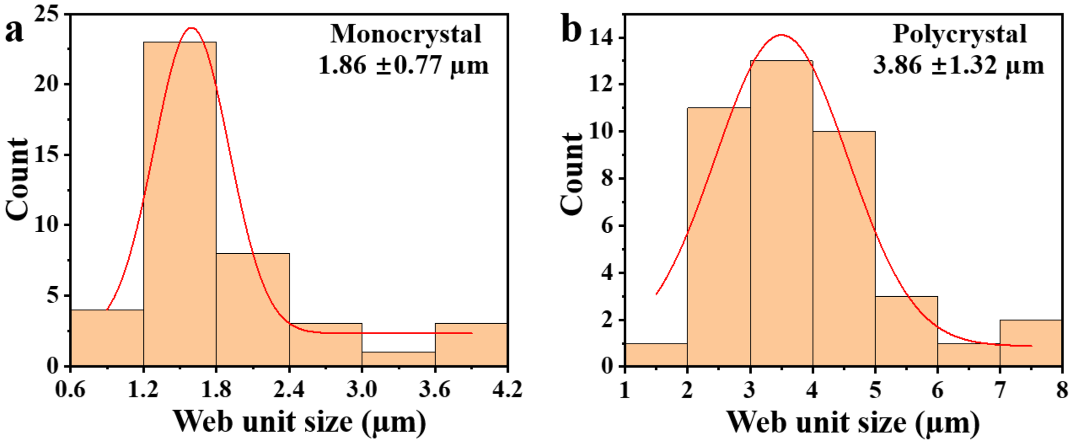

Fig. S9 Histogram of web unit size distribution obtained from the SEM images shown in Fig. S8 a and Fig. S7 b, respectively.

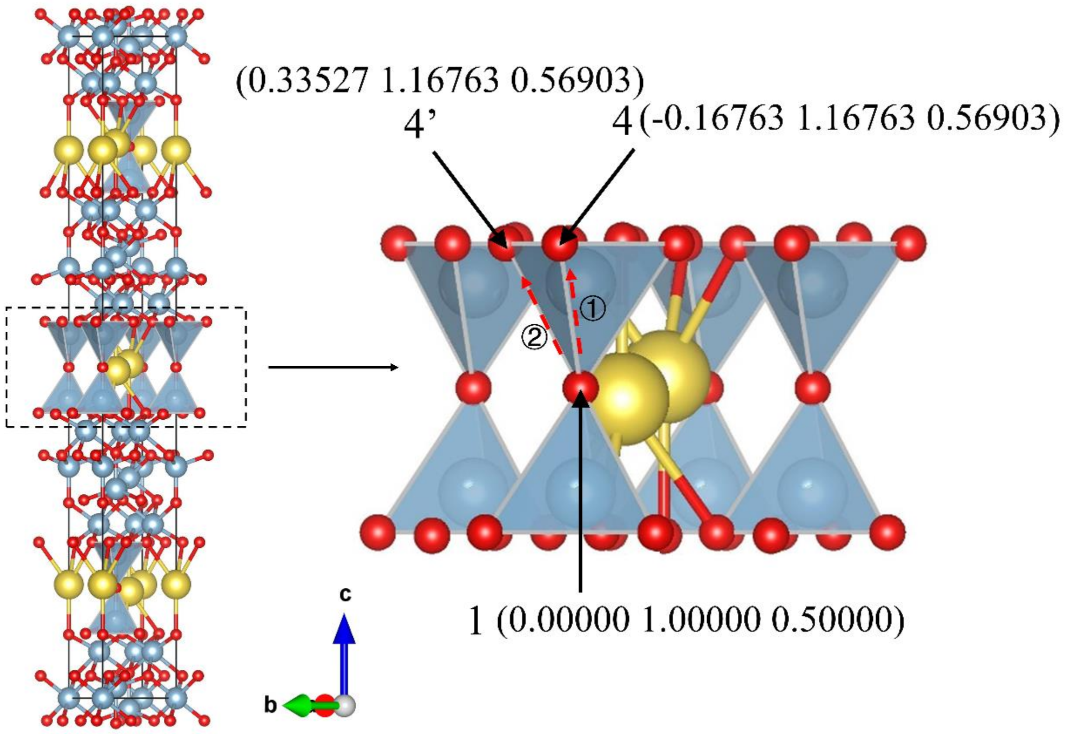

Fig. S10 Structure model of β''-Al_2O_3. (a) Crystal structure of β″-Al_2O_3 with a space group R3m and lattice constants of a = 5.61 Å and c = 33.74 Å in a hexagonal setting. The magnified view on the right shows two atom shift paths (denoted by two red-dashed arrows: route ①, 1-4; route ②, 1-4') leading to closure of the Na^+ conduction channels. Red, blue and yellow represent O, Al and Na atoms, respectively.

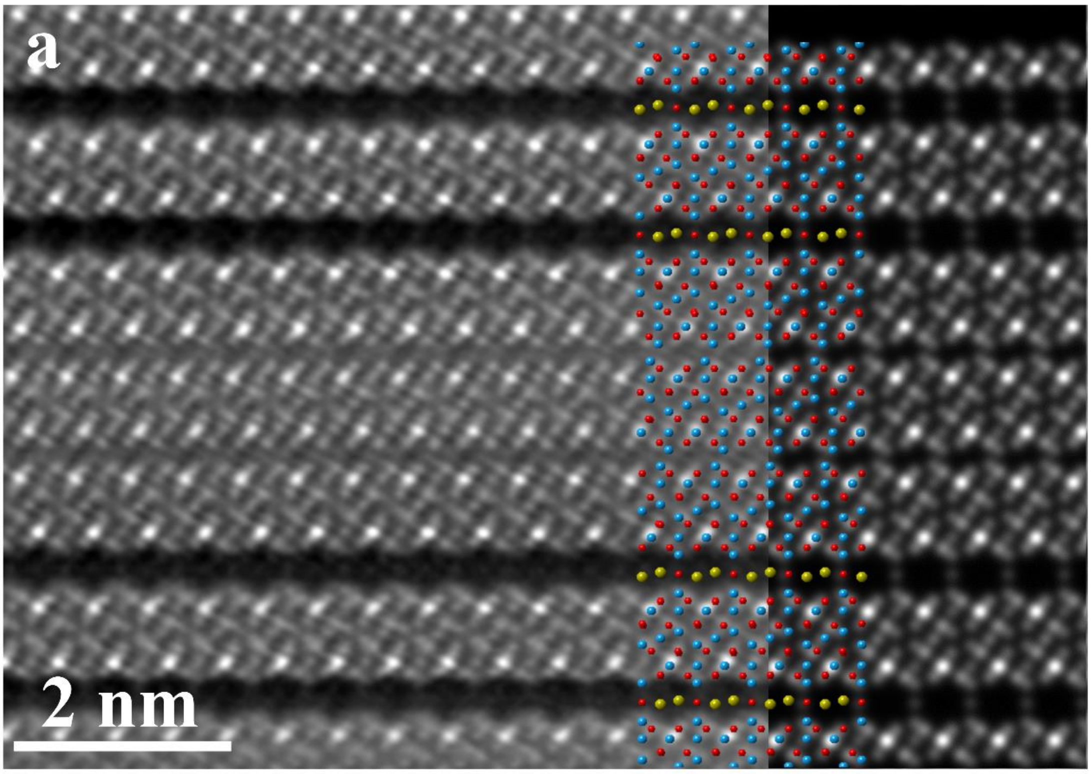

Fig. S11 Atomic scale HAADF image of the conduction planes closure in β''-Al_2O_3 SE caused by electrochemical cycling. (a) Atomic scale HAADF image of the β''-Al_2O_3 grain with several Na^+ conduction planes being closed, and the simulated HAADF image (right) matches well with the experimental HAADF image. Red, blue and yellow represent O, Al and Na atoms, respectively.

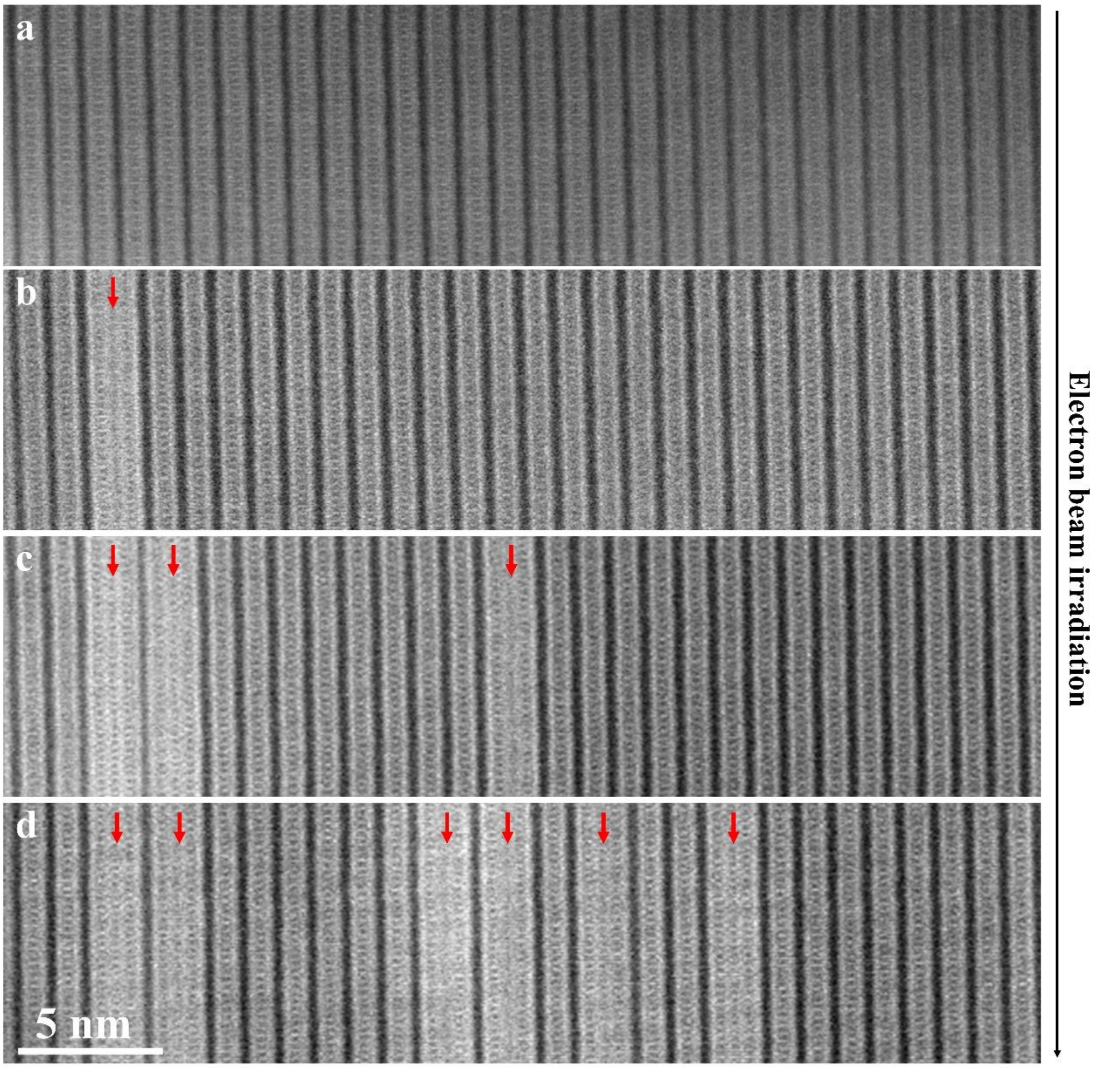

Fig. S12 HAADF images showing conduction plane closure induced by electron beam irradiation. (a) A HAADF image of β″- Al_2O_3 without electron beam irradiation. (b-d) As the irradiation time increases, many Na^+ conduction planes in β″- Al_2O_3 were closed.

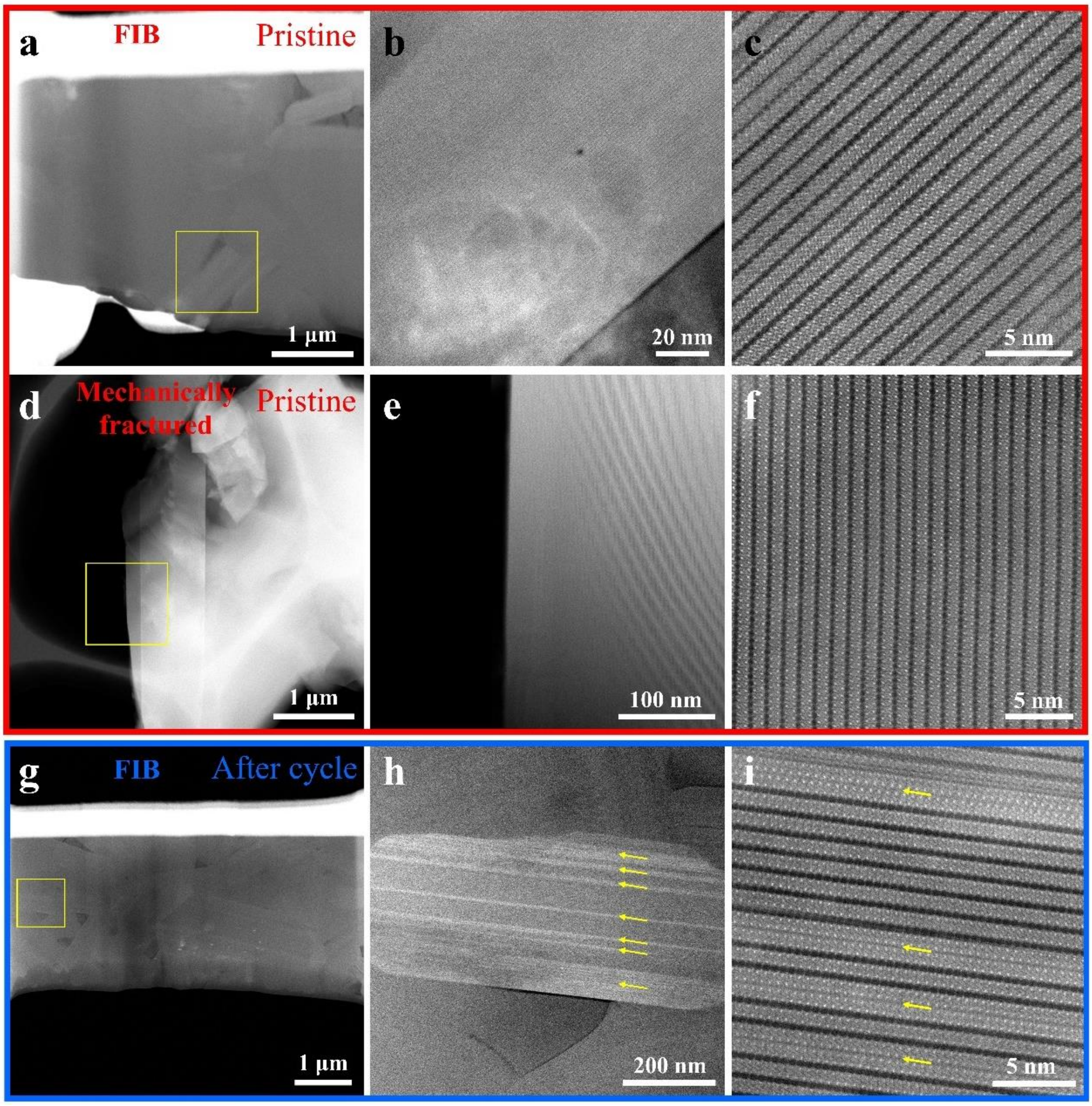

Fig. S13 HAADF characterization of β''-Al_2O_3 SE before and after *in situ* OM cycling. (a) Low magnification HAADF image of the FIB processed pristine β''-Al_2O_3 grain. (b, c) Magnified view of the pristine β''-Al_2O_3 grain corresponding to the boxed regions in (a). (d) Low magnification HAADF image of the mechanically crushed pristine β''-Al_2O_3 grain. (e, f) Magnified view of the pristine β''-Al_2O_3 grain corresponding to the boxed regions in (d). (g) Low magnification HAADF image of the FIB processed cycled β''-Al_2O_3 grain. (h, i) Magnified view of the β''-Al_2O_3 grain corresponding to the boxed regions in (g), showing the closure of the conduction planes (marked by yellow arrows).

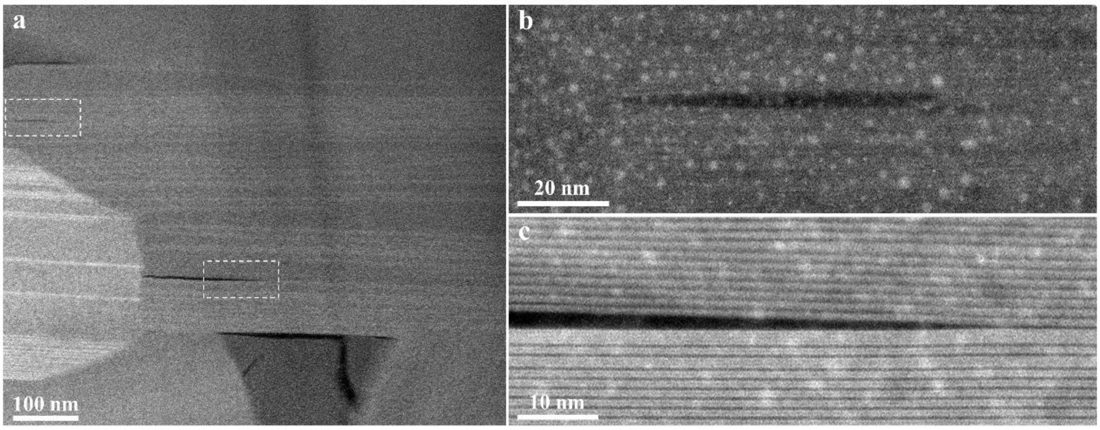

Fig. S14 HAADF characterization of delamination cracks in β''-Al_2O_3 SE after cycling. (a) Low magnification HAADF image of delamination cracks in a β''-Al_2O_3 grain. (b, c) Magnified view of the delamination cracks corresponding to the boxed regions in (a).

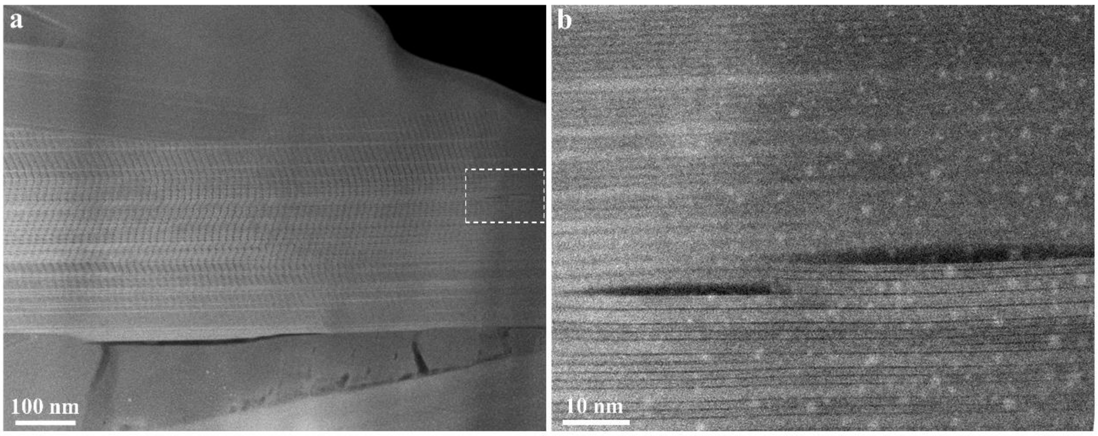

Fig. S15 HAADF characterization of delamination cracks in β''-Al_2O_3 SE after cycling. (a) Low magnification HAADF image of delamination cracks in a β''-Al_2O_3 grain. (b) Magnified view of the delamination cracks corresponding to the boxed region in (a).

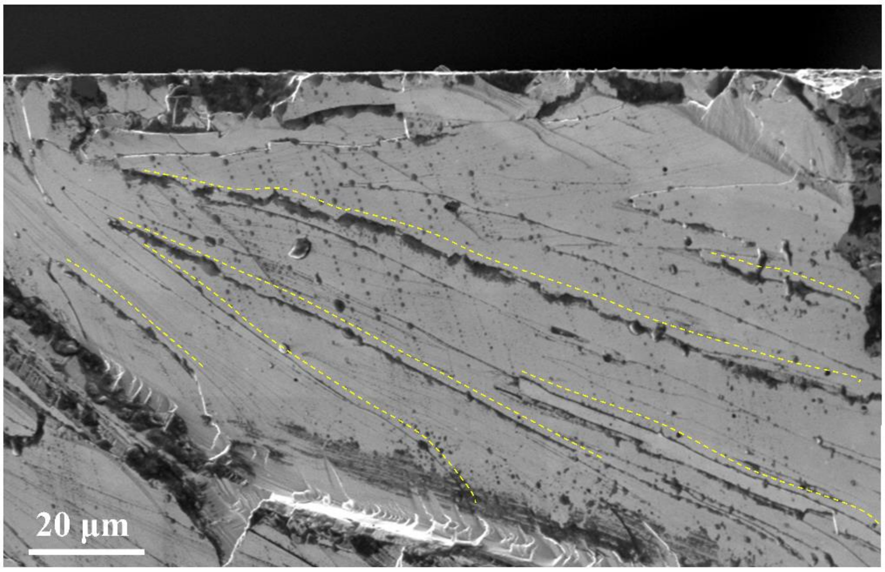

Fig. S16 SEM image showing Na-filled delamination cracks (outlined by yellow dotted lines).

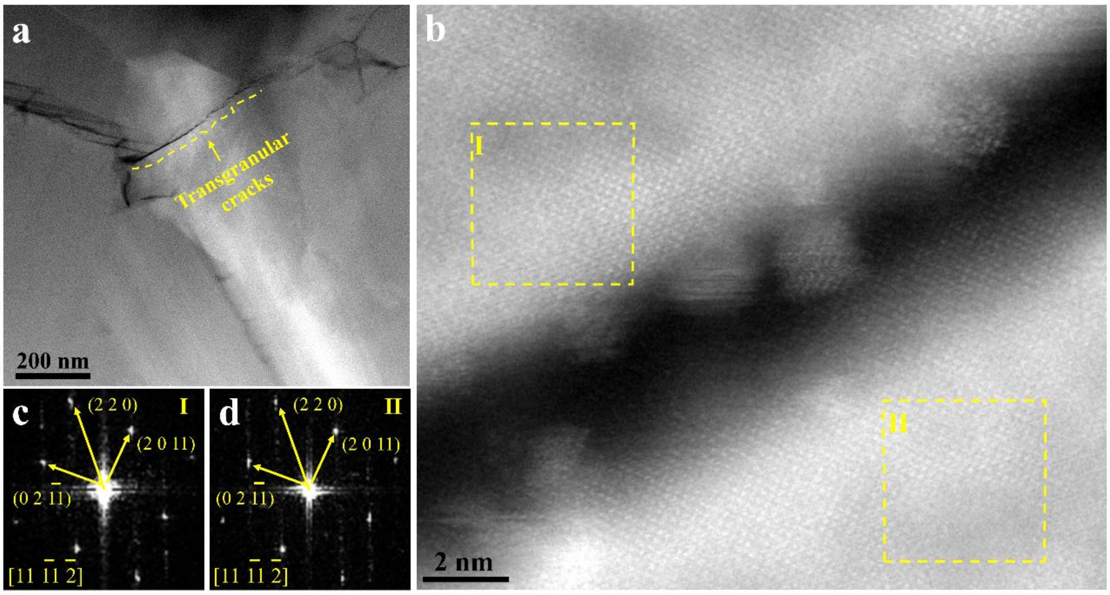

Fig. S17 HAADF characterization of the transgranular crack in β''-Al_2O_3 SE after optical cycling. (a) Low magnification HAADF image of a transgranular crack (outlined by a yellow dotted line). (b) Atomic scale imaging of the transgranular crack in (a). (c, d) Fast Fourier transform (FFT) of the β''-Al_2O_3 grain on both sides of the crack, corresponding to the region boxed by yellow dotted lines in (b), confirming the transgranular crack.

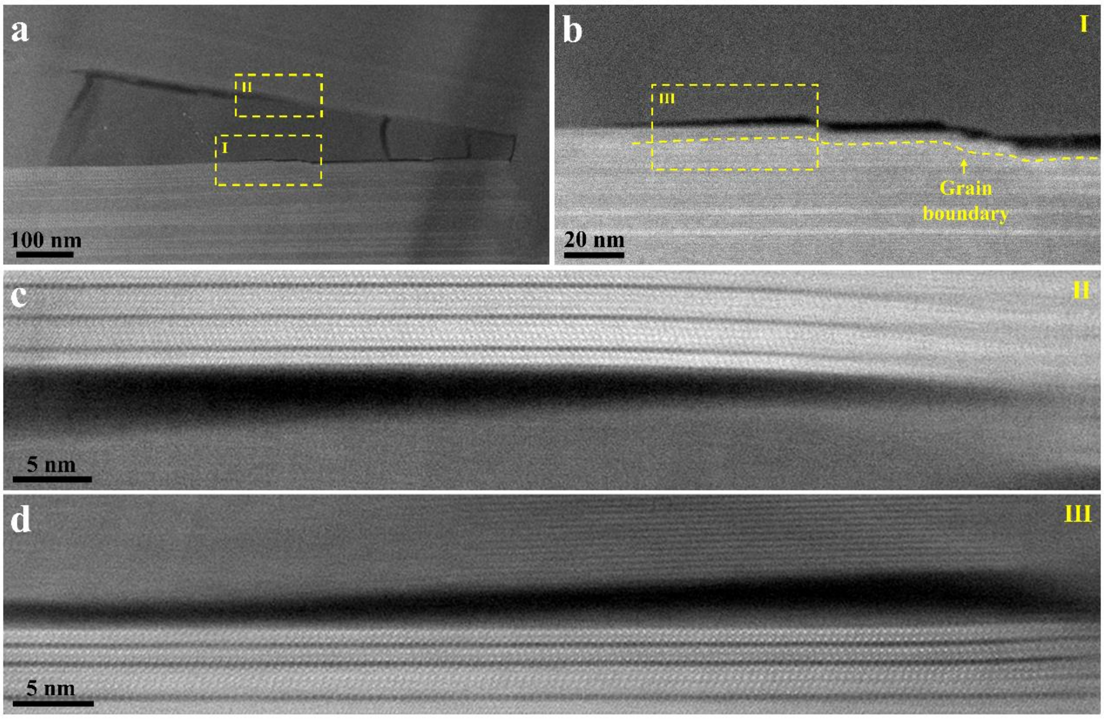

Fig. S18 HAADF characterization of the intergranular crack in β''-Al_2O_3 SE after cycling. (a) Low magnification HAADF image of intergranular cracks. (b) Magnified view of the grain boundary corresponding to the box Ⅰ in (a). (c) Atomic scale imaging of the grain boundary corresponding to the box Ⅱ in (a). (d) Atomic scale imaging of the grain boundary corresponding to the box Ⅲ in (b).

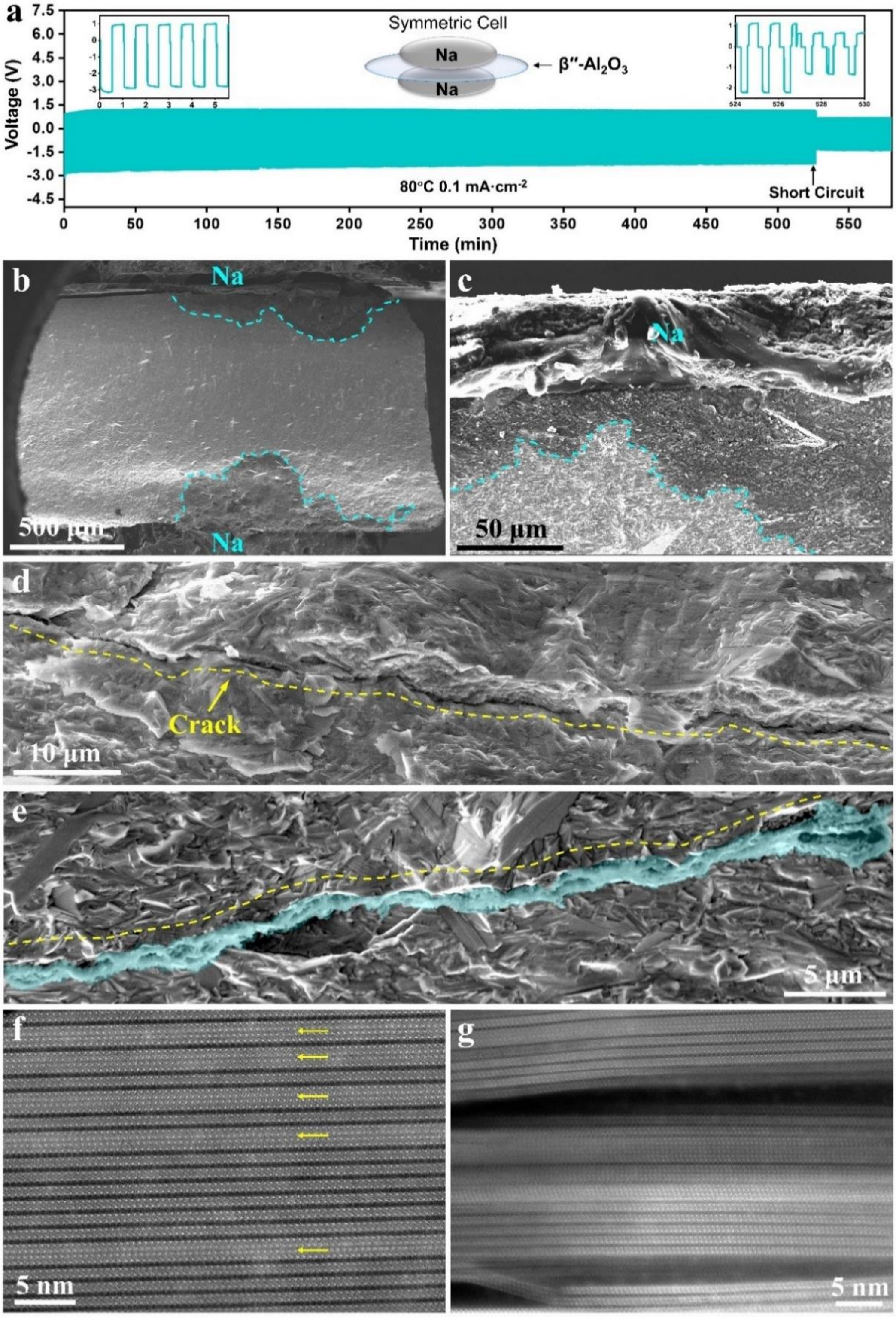

Fig. S19 Na dendrite growth in Na/β''-Al_2O_3/Na actual symmetric cell. (a) Galvanostatic cycling with a current density of 0.1 mA/cm^2 at 80 °C. (b-e) SEM images of the β''-Al_2O_3 SE after electrochemical cycling. The blue-dashed lines in (b) and (c) trace the Na plating paths. The yellow-dashed lines in (d) and (e) trace the crack path. (f-g) HAADF-STEM images of delamination cracks and closure of the conduction planes in β''-Al_2O_3 SE after electrochemical cycling.

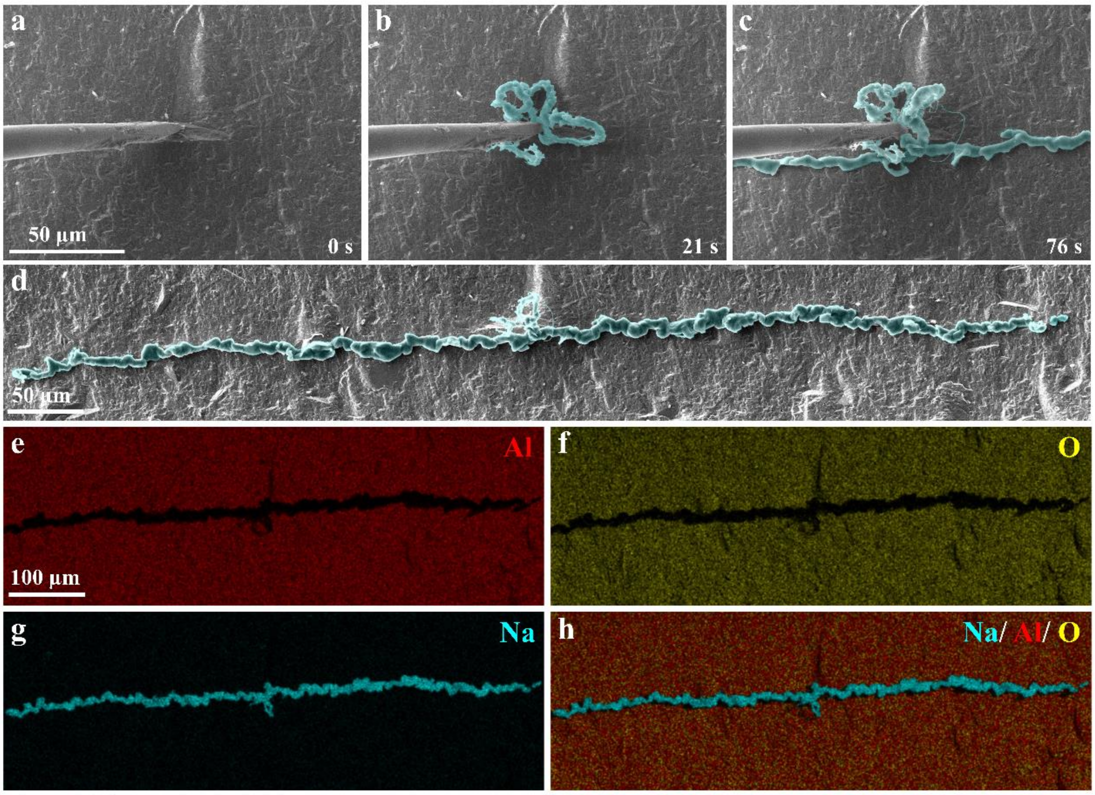

Fig. S20 *In situ* SEM observation of Na deposition and cracking in β''-Al_2O_3 SE in a mesoscale ASSB. (a-c) Time-lapse images showing the formation of a long horizontal crack. Dendrites grew around the W tip (b) and induced a horizontal crack (c). (d) A full view of the crack. (e-h) Elemental mapping images of the Na filled crack in β''-Al_2O_3 SE.

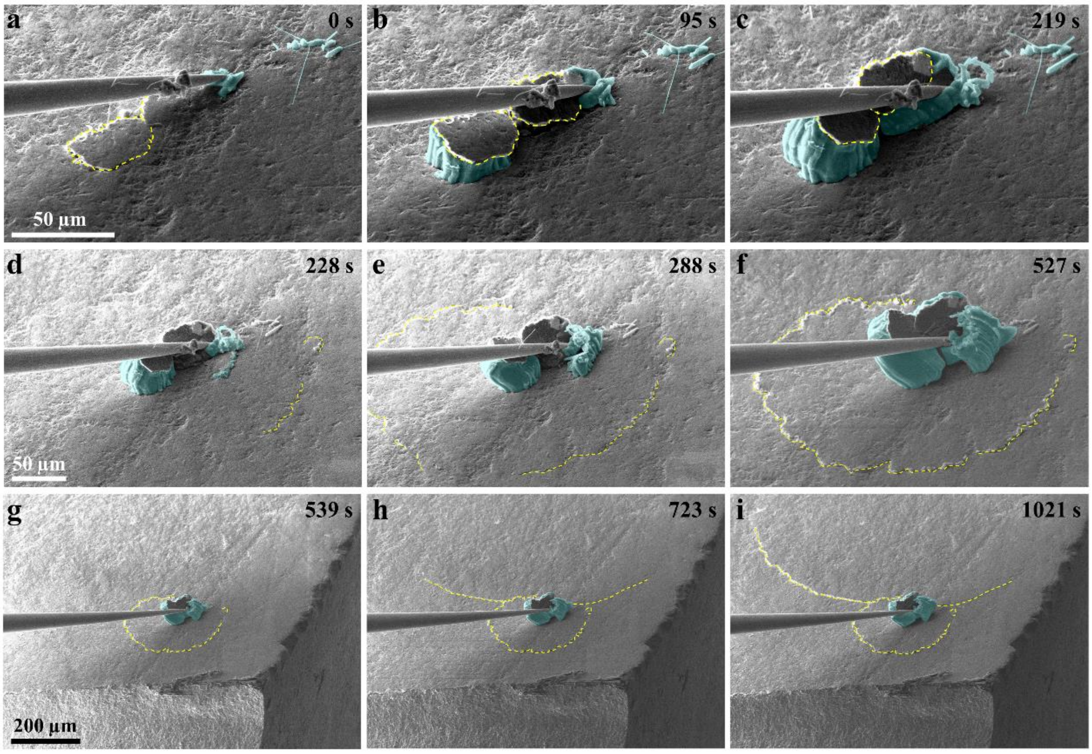

Fig. S21 ***In situ*** **SEM observation of Na deposition and cracking in β''-Al_2O_3 SE in a mesoscale ASSB.** (a-i) Time-lapse images showing the formation of a bowl-shaped crack. (a-c) Na deposited and lifted two sheets of SE. (d-i) Na deposition and formation of a bowl-shaped crack.

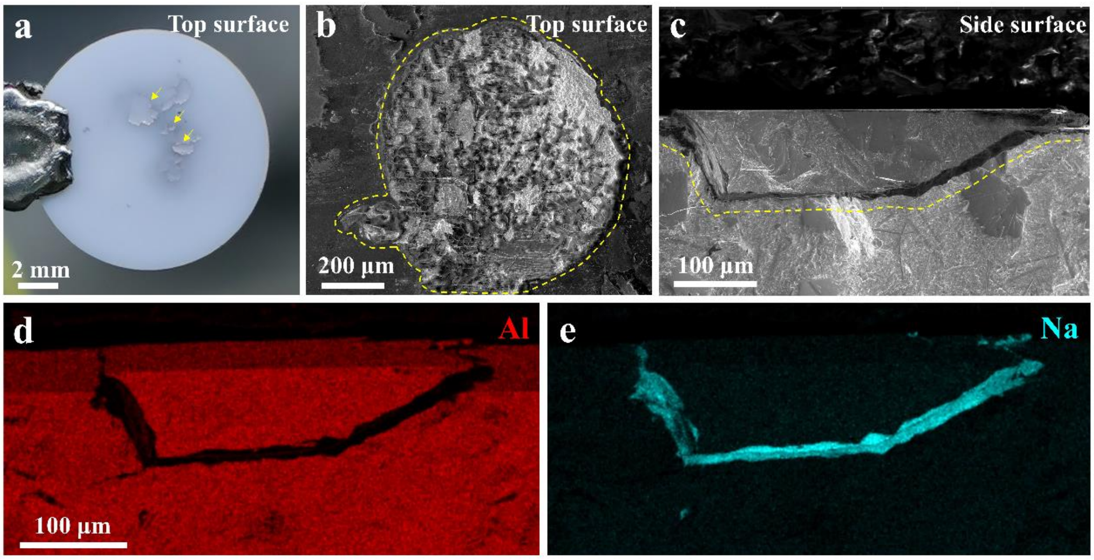

Fig. S22 Morphology of the β''-Al_2O_3 SE after cycling. (a) Optical microscopy image showing many sheets of SE lifted off by Na deposition (marked by yellow arrows). (b) SEM images showing the top surface of "bowl-shaped" crack (outlined by yellow dashed lines). (c-e) SEM image with the corresponding elemental mappings showing the side surface of "bowl-shaped" crack (outlined by yellow dotted lines).

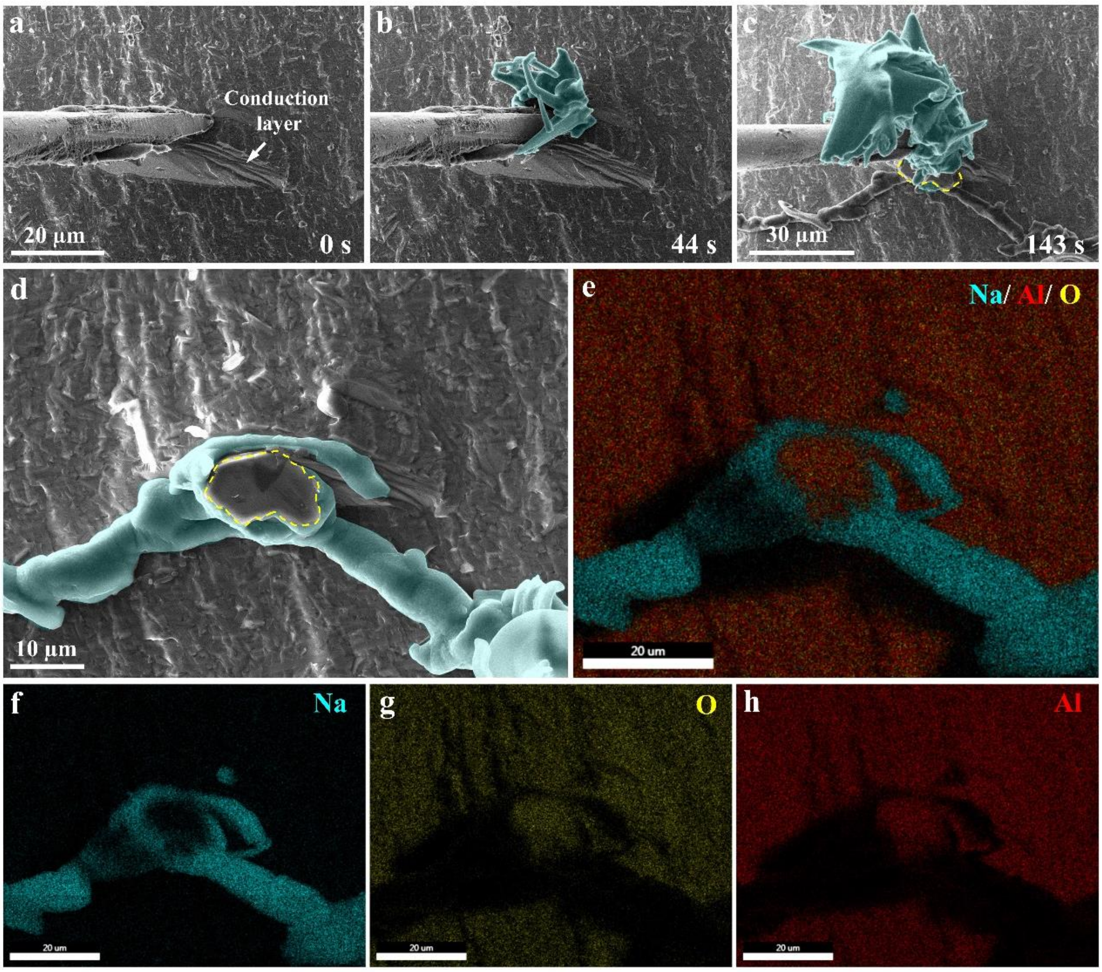

Fig. S23 *In situ* SEM observation of Na deposition and cracking in β''-Al_2O_3 SE in a mesoscale ASSB. (a-c) Time-lapse images showing a sheet-like β''-Al_2O_3 SE pushed up by Na metal. (d) High magnification SEM images showing Na extruded out of the Na^+ conduction layer of β''-Al_2O_3 single crystal grain. (e-h) Elemental mapping images of the Na dendrite in the β''-Al_2O_3 SE.

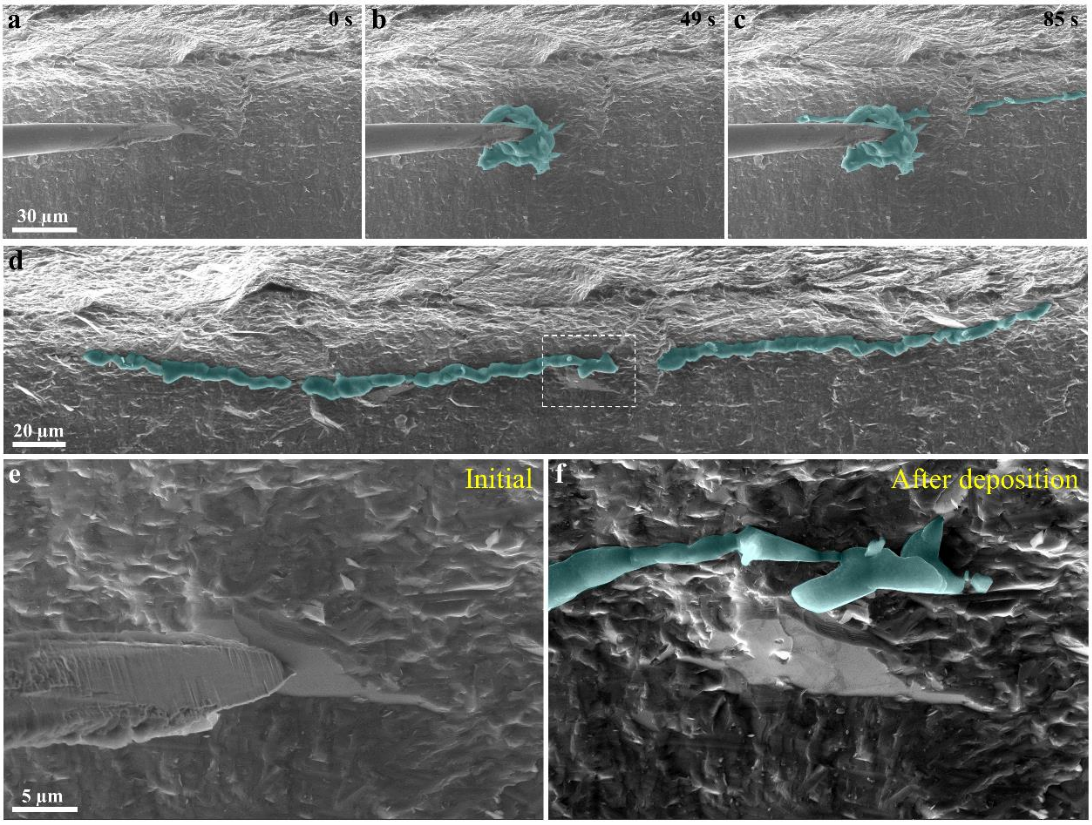

Fig. S24 ***In situ*** **SEM observation of Na deposition and cracking in β''-Al_2O_3 SE in a mesoscale ASSB.** (a-c) Time-lapse images showing the formation of a horizontal crack. Dendrites grew around the W tip (b) and induced a horizontal crack. (d) A full view of the crack. (e) High magnification SEM image of a grain before battery test, with the Na^+ conduction layers clearly visible. (f) High magnification SEM image of a grain after battery test showing Na metal extruded out from the conduction layer.

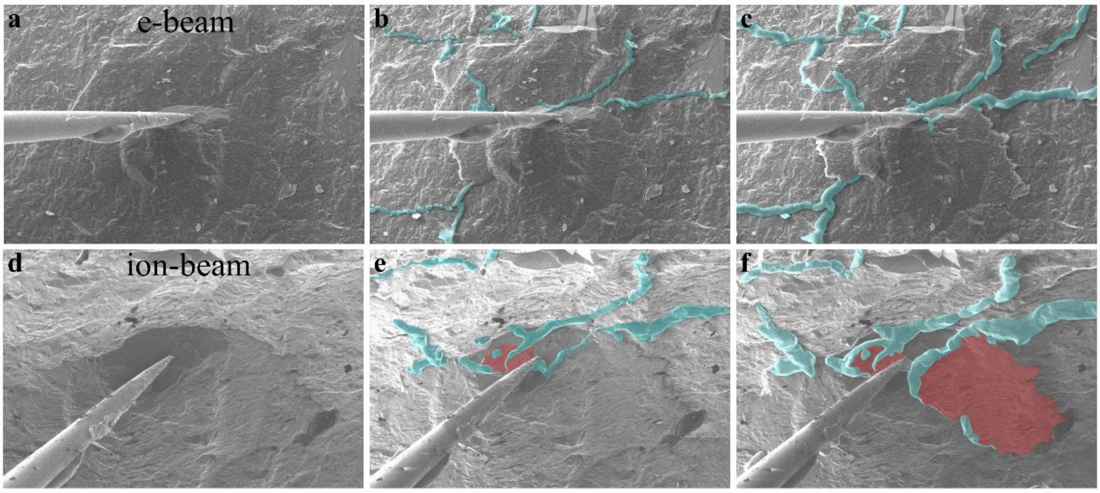

Fig. S25 ***In situ*** **SEM observation of Na deposition and cracking in β''-Al$_2$O$_3$ SE in a mesoscale ASSB.** (a-c) SEM images showing the formation of cracks. (d-f) Ion beam images showing the formation of cracks corresponding to (a-c). With the further deposition, sheet electrolyte (marked in red) was pushed up by Na metal.

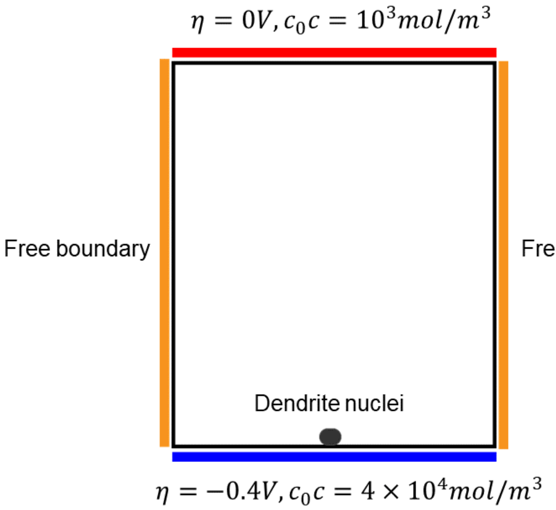

Fig. S26 Boundary conditions in numerical implementation. Dirichlet boundary conditions are used for ions concentration and electrical potential on the top and bottom edges. Free boundary conditions are adopted for other fields.

Numerical section

A multiscale, multiphysics model based on the phase-field method is developed to investigate the delamination crack within polycrystalline grains and the dendrite morphological evolution. All independent variables are functions of three dimensions space $\boldsymbol{x}$ and time t. We employ $\xi(\boldsymbol{x},t)$ as the sodium metal phase to distinguish sodium dendrite ($\xi=1$) and solid electrolytes ($\xi=0$), $\eta(\boldsymbol{x},t)$ as the electrical potential that drives ions migration, $d(\boldsymbol{x},t)$ as the crack phase to describe the damaged area ($d=1$) and undamaged region ($d=0$), $c(\boldsymbol{x},t)$ as the dimensionless Na^+ concentration which is normalized by the Na^+ bulk concentration (c_0) within the SEs and $\boldsymbol{u}(\boldsymbol{x},t)$ as the displacement. The total free energy functional of the system is formulated as

$$\mathcal{F}=\int\left[f_{\mathrm{chem}}+f_{\mathrm{grad}}+f_{\mathrm{elec}}+f_{\mathrm{mech}}+f_{\mathrm{crack}}\right]\mathrm{d}V, \tag{1}$$

where f_{chem}, f_{grad}, f_{elec}, f_{mech} and f_{crack} are chemical, gradient, electric, mechanical and crack surface energy density, respectively. The chemical energy density is adopted as

$$f_{\mathrm{chem}}(c,\xi)=c_0c\mu_c^0+c_0RTc\ln c+W\xi^2(\xi-1)^2, \tag{2}$$

where μ_c^0 is the standard chemical potential of Na^+, $R=8.314J/(K\cdot mol)$ is the gas constant, T means room temperature and W is phenomenological parameter that describes the barrier height of the double-well function. The first and second term in Eq. (2) describes the chemical energy caused by Na^+, and the last term represents the contribution from Na dendrite. Gradient energy density is formulated as

$$f_{\mathrm{grad}}(\nabla\xi,\nabla\eta)=\frac{\kappa_\xi}{2}(\nabla\xi)^2-\frac{\kappa_\eta}{2}(\nabla\eta)^2, \tag{3}$$

where κ_ξ is gradient energy coefficient corresponding to the surface energy of Na metal and $\kappa_\eta=h(\xi)\kappa_\eta^{\mathrm{me}}+(1-h(\xi))\kappa_\eta^{\mathrm{el}}$ is electric permittivity where $h(\xi)=\xi^3(6\xi^2-15\xi+10)$ is an interpolated function. In addition, $\kappa_\eta^{\mathrm{me}}$ and $\kappa_\eta^{\mathrm{el}}$ are electric permittivity of metal and electrolytes, respectively. Electric energy density is described as

$$f_{\mathrm{elec}}(c,\eta)=c_0cF\eta, \tag{4}$$

where $F=96485C/mol$ is the Faraday constant and c_0cF represents the charge density of Na^{+}. Only elastic strain energy density is taken into the mechanical energy density because the plastic deformation of β''-Al$_2$O$_3$ is negligible. Then the mechanical energy density is decomposed as the tensile strain energy density (ψ^{+}) and compressive strain energy density (ψ^{-}), the corresponding formula is

$$f_{\text{mech}}(\xi, d, u_i) = [(1-d)^2 + k]\psi^{+}(\xi, u_i) + \psi^{-}(\xi, u_i), \tag{5}$$

where k is a small positive number to avoid singularity in numerical simulation.[1, 2] When crack extension takes place, the tensile strain energy will be released but the compressive strain energy is still there because only the tensile strain energy is the driving force for crack propagation. The crack surface energy density is formulated as

$$f_{\text{crack}}(\xi, d) = \frac{g_c}{2l}[d^2 + l^2(\nabla d)^2], \tag{6}$$

where g_c is the Griffith-type critical energy release rate and it is given by $g_c = h(\xi)g_c^{\text{me}} + (1-h(\xi))g_c^{\text{el}}$, l is a length-scale parameter that regularize the sharp crack. Again, only the tensile strain energy density is the driving force for crack propagation and crack extension can release the local stress to reduce the mechanical energy.

The evolution of Na dendrite and crack propagation can be obtained by solving the Allen-Cahn equations[3] as

$$\frac{\partial \xi}{\partial t} = -L_{\xi}\mu_{\xi}$$

$$-L_{\eta}h'(\xi)\left[-c\exp\left(\frac{-1}{2RT}\left(F\eta - \frac{\sigma_{kk}}{3}\Omega_{\text{Na}}\right)\right) + \exp\left(\frac{1}{2RT}\left(F\eta - \frac{\sigma_{kk}}{3}\Omega_{\text{Na}}\right)\right)\right] \quad (7-1)$$

$$\mu_{\xi} = \frac{\delta f_{\text{chem}}}{\delta \xi} + \frac{\delta f_{\text{grad}}}{\delta \xi} = 4W\xi(\xi - 0.5)(\xi - 1) - \kappa_{\xi}\nabla^2\xi, \quad (7-2)$$

and

$$\frac{\partial d}{\partial t} = -L_d\mu_d \quad (8-1)$$

$$\mu_d = \frac{\delta f_{crack}}{\delta d} + \frac{\delta f_{mech}}{\delta d} = \frac{g_c}{l}(d - l^2\nabla^2 d) - 2(1-d)\max_t[\psi^{+}(\xi, u_i)], \quad (8-2)$$

here L_{ξ} is interface mobility, L_{η} is rate constant and $\Omega_{\text{Na}} = 24 \times 10^{-6} m^3/mol$ is the molar volume of Na. In Eq. (7-1), the first term represents evolution driven by the interface energy, and the second term follows Butler-Volmer kinetics where the reaction rate is exponentially to the overpotential and pressure. The operator $\max_t[\cdot]$ means the maximum value during evolution time t and L_d is reciprocal of the viscosity of β''-

Al_2O_3. On the right side of Eq. (8-2), the first term is the resistant force due to fracture toughness and the second term represents the crack driving force resulted from the elastic tensile strain energy density. Mass transfer of Na^+ obeys

$$\frac{\partial c}{\partial t} = \nabla \cdot (\mathrm{M}c\nabla\mu_c) - \frac{c_s}{c_0}\frac{\partial \xi}{\partial t} \qquad (9-1)$$

$$\mu_c = \mu_c^0 + \mathrm{RT}(1 + \ln c) + F\eta, \qquad (9-2)$$

where M is the mobility of Na^+ and $c_s = 4 \times 10^4 mol/m^3$ is the site density of Na metal. In Eq. (9-1), the first term describes diffusion and migration of Na^+, and the second term means the consumption/generation of Na^+ during chemical reaction. Mechanical equilibrium and charge neutrality are also assumed in our model to simulate the stress and electric potential distribution. Compared with the proposed model [4, 5]for dendrite growth in liquid electrolytes, our model also contains 1. the mechanical energy due to the deposited dendrite and deformation of the SEs 2. the fracture energy of the electrolytes due to crack extension. Furthermore, the fracture model used in our model is thermodynamically consistent and numerically robust.[1, 2]

For the sake of simplicity, two special treatments are adopted in simulation. Firstly, the grain boundary (GB) effect on crack propagation is not taken into consideration. In experimental conditions, the fracture toughness along the conduction channels and the GBs is lower than other directions, thus both channels and GBs could be the path for the crack extension. As we only focus on the mechanism and evolution of the delaminated crack inside the grains, the intergranular fracture is not studied here. Secondly, the physical properties of SEs are taken as homogeneous and isotropic in macroscale simulation. Despite the properties of grains are anisotropic, this assumption is still reasonable considering the grain size is much smaller than the battery size. The stress effect on electrodeposition at each macro point reflects the stress state of each micro grain, and this stress fluctuates during dendrite growth and crack propagation. To accelerate numerical computational process, a predefined fluctuation is adopted at each macro point and this fluctuation can affect the overpotential according to Butler-Volmer kinetics in Eq. (7-1).

Our numerical simulation is implemented in COMSOL Multiphysics 6.0 and the corresponding computational parameters are listed in Table. S1. In addition, bulk concentration c_0 is taken as $1 \times 10^3 mol/m^3$ and length-scale parameter l is $10nm$. Figure S19 shows the boundary conditions in simulation for delaminated crack and fractal dendrite. The average length of grains is $2.5\mu m$ and the size of the battery is $4 \times 4mm^2$. Energy release rate along the conduction channels is a hundred times smaller than the perpendicular direction. Triangle meshes are adopted to discrete the simulation domain where the minimum mesh size is $1nm$ in crack simulation and $10\mu m$ in dendrite simulation.

Table S1. Phase field simulation parameters in numerical implementation.

	symbol	unit	Na	β"-Al_2O_3
Interface mobility	L_ξ	$m^3/(J \cdot s)$	2.5×10^{-6}	
Reaction constant	L_η	$1/s$	0.2	
Barrier height	W	J/m^3	6.24×10^4	
Gradient coefficient	κ_ξ	J/m	2×10^{-5}	
Na^+ Diffusion coefficient	D	m^2/s	10^{-15}	10^{-13}
relative permittivity	ϵ_r		1000	3
Young's modulus	E	GPa	9	290
Poisson's ratio	v		0.31	0.24
Energy release rate	g_c	kJ/m^2	12	0.05

References

1. C. Miehe, F. Welschinger and M. Hofacker, *International Journal for Numerical Methods in Engineering*, 2010, **83**, 1273-1311.
2. C. Miehe, L.-M. Schänzel and H. Ulmer, *Computer Methods in Applied Mechanics and Engineering*, 2015, **294**, 449-485.
3. L.-Q. Chen, *Annual Review of Materials Research*, 2002, **32**, 113-140.
4. L. Chen, H. W. Zhang, L. Y. Liang, Z. Liu, Y. Qi, P. Lu, J. Chen and L.-Q. Chen, *Journal of Power Sources*, 2015, **300**, 376-385.
5. L. Liang and L.-Q. Chen, *Applied Physics Letters*, 2014, **105**, 263903.